

300 years of sclerosponge thermometry shows global warming has exceeded 1.5 °C

Received: 19 May 2023

Accepted: 19 December 2023

Published online: 5 February 2024

 Check for updates

Malcolm T. McCulloch ^{1,2}✉, Amos Winter ³, Clark E. Sherman ⁴ & Julie A. Trotter ¹

Anthropogenic emissions drive global-scale warming yet the temperature increase relative to pre-industrial levels is uncertain. Using 300 years of ocean mixed-layer temperature records preserved in sclerosponge carbonate skeletons, we demonstrate that industrial-era warming began in the mid-1860s, more than 80 years earlier than instrumental sea surface temperature records. The Sr/Ca palaeothermometer was calibrated against ‘modern’ (post-1963) highly correlated ($R^2 = 0.91$) instrumental records of global sea surface temperatures, with the pre-industrial defined by nearly constant ($<\pm 0.1$ °C) temperatures from 1700 to the early 1860s. Increasing ocean and land-air temperatures overlap until the late twentieth century, when the land began warming at nearly twice the rate of the surface oceans. Hotter land temperatures, together with the earlier onset of industrial-era warming, indicate that global warming was already 1.7 ± 0.1 °C above pre-industrial levels by 2020. Our result is 0.5 °C higher than IPCC estimates, with 2 °C global warming projected by the late 2020s, nearly two decades earlier than expected.

Global warming is causing major changes to the Earth’s climate¹, with heatwaves of unprecedented scale occurring across southern Europe, China and large parts of North America². Furthermore, during the 2023 Northern Hemisphere summer, heatwaves occurred towards the end of a prolonged La Niña cool phase, when global mean temperatures were below the long-term warming trend. This and the switch of ENSO (El Niño/Southern Oscillation) to a warmer-than-average El Niño phase in 2023–24, means that intense heatwaves and associated extreme events may now be the new normal. This questions whether global mean surface temperatures (GMSTs) have, or will soon exceed, the Paris Agreement of 2015 of holding GMSTs to “well below 2 °C above pre-industrial levels and pursuing efforts to limit the temperature rise to no more than 1.5 °C above pre-industrial levels”³.

To address this question and whether even more extreme events are likely in the near future⁴ requires knowledge of the total magnitude of global warming that has occurred since the pre-industrial period. The pre-industrial-period is defined as the stable “mean climate state just

before human activities started to demonstrably change the climate through combustion of fossil fuels”⁵. Given that anthropogenic concentrations of atmospheric CO₂ started to increase in the early 1800s⁶, the pre-industrial reference period should ideally be defined well before this, in the mid-1700s or earlier. Complicating this requirement is the series of exceptionally large volcanic eruptions in the early 1800s that caused global-scale cooling of unprecedented levels in recent living history⁷. Most limiting, however, is that instrumental ship-based records of global sea surface temperature (SST) only began in the 1850s and then with limited coverage (Extended Data Fig. 1)^{8,9}. Thus, for pragmatic reasons¹⁰, the earliest available instrumental records from 1850 to 1900 have been used to define the IPCC ‘pre-industrial’ period. The instrumental record of GMST is therefore constructed from the areal weighted average of SST, blended with land-air temperatures^{11,12}, the latter extending back to the 1750s¹² but with larger uncertainties. For global SSTs, the most widely used products (for example, HadSST4 (ref. 13) and ERSST5 (ref. 14)) rely on the International Comprehensive

¹Oceans Graduate School and UWA Oceans Institute, The University of Western Australia, Crawley, Western Australia, Australia. ²ARC Centre of Excellence in Coral Reef Studies, The University of Western Australia, Crawley, Western Australia, Australia. ³Earth and Environmental Systems Department, Indiana State University, Terre Haute, IN, USA. ⁴Department of Marine Sciences, University of Puerto Rico-Mayaguez, Mayaguez, PR, USA.

✉e-mail: Malcolm.McCulloch@uwa.edu.au

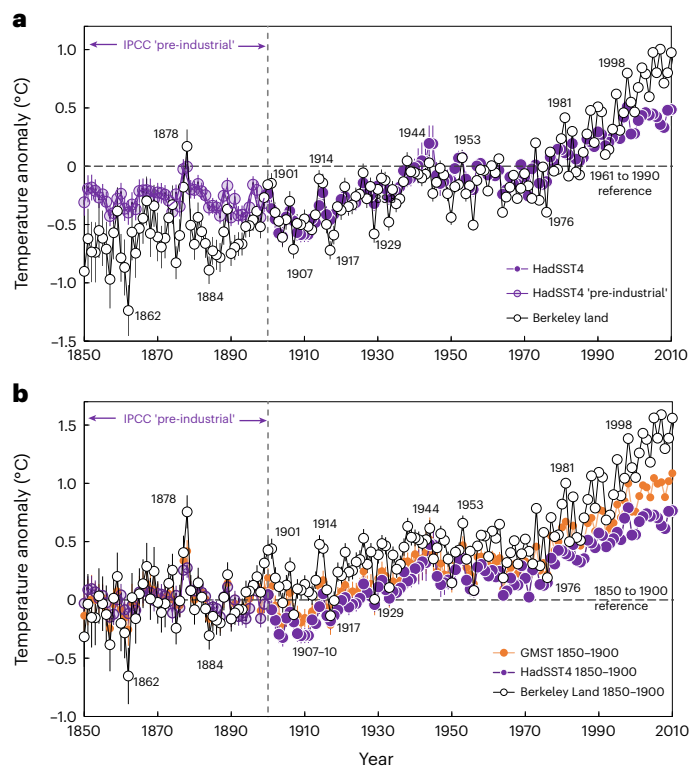


Fig. 1 | Global sea surface and land-air temperature anomalies since 1850.

a, Anomalies referenced to the 1961–1990 average with HadSST4 (ref. 13) being consistently warmer than land-air temperatures^{11,12} from 1850 to 1900. **b**, Anomalies referenced to the IPCC 1850–1900 pre-industrial period^{10,16} with anomalous cooling of SSTs relative to the land from the early 1900s. Global warming (GMST) is the weighted mean of land-air (~32%) and sea surface (~68%) temperatures. Uncertainties represent the 95% confidence interval^{11–13}.

Ocean Atmosphere Data Set (ICODAS)¹⁵, with the denser network of ‘modern’ reliable observations beginning in the second-half of the twentieth century^{8,9}.

The limitations of these products are evident when the earliest available global SSTs¹³ are compared (Fig. 1) with the land-air temperatures^{11,12}. When normalized to the ‘modern’ 1961–1990 anomaly reference period, the records overlap closely from about 1900 to the 1980s (Fig. 1a), with generally warmer land temperatures during El Niño and cooler temperatures during La Niña phases. However, the records diverge markedly between 1850 and 1900, when SSTs are warmer (~0.3 °C) than the land, except during the very strong El Niño of 1877–78 (Fig. 1a). This is a conundrum because in a stable state, changes in land temperatures should closely track those in the much higher heat capacity upper oceans, as has occurred for most of the twentieth century (Fig. 1a). Consequently, when ocean and land anomalies are instead referenced to the IPCC 1850–1900 pre-industrial period¹⁰, SSTs are apparently ~0.3 °C cooler than the land from the early 1900s, an offset that continues to the 1980s, then increases further as part of the late-twentieth-century enhanced warming of the land (Fig. 1b)¹⁶. In addition to there being no plausible explanation for such an abrupt cooling of the oceans in the early 1900s while the land continued to warm, this inconsistency has important implications for the processes responsible for the now even faster rates of late-twentieth-century land warming. For example, is the accelerated warming of the land since the 1990s^{11,12} due to a major regime shift in climate (Fig. 1a) or is it part of the same long-term warming trend shown when records are referenced to the IPCC 1850–1900 pre-industrial period¹⁰ (Fig. 1b)?

To resolve this question, here we report an extended 300 yr Sr/Ca palaeotemperature record preserved in the calcium carbonate

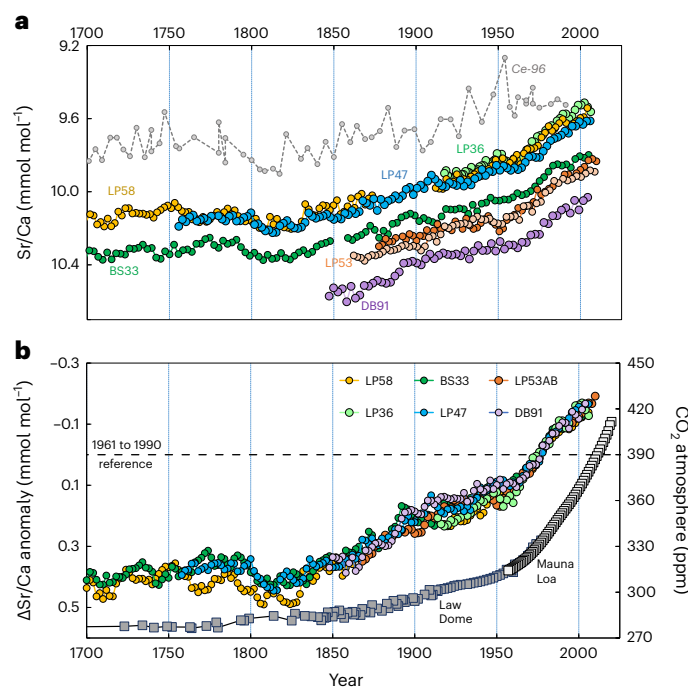


Fig. 2 | Sr/Ca temperature records from Caribbean sclerosponges. **a**, Sr/Ca ratios (mmol mol⁻¹) from the aragonite skeletons sampled at continuous ~2 yr (0.5 mm) intervals from the years 2012 back to 1700. Specimens were collected from OML depths of 33–91 m offshore Puerto Rico and St Croix. Published²⁵ lower-resolution sclerosponge Sr/Ca analyses (Ce-96 grey symbols) collected²⁵ from within the OML. **b**, Stacked Δ Sr/Ca anomalies referenced to 1961–1990 means (Methods). Right axis shows atmospheric CO₂ records from Mauna Loa⁴¹ (open symbols) and the Law Dome⁶ ice core (filled symbols).

skeletons of long-lived sclerosponges. Live specimens were collected from the Caribbean at depths between 33 and 91 m, within the ocean mixed-layer (OML), the region where heat is exchanged between the atmosphere and the ocean interior⁹. Here, the thermal gradient is homogenized by turbulent mixing from the sea surface to the base of the OML, with its much greater thermal inertia providing a more stable, representative record of upper surface ocean temperatures compared to the highly variable uppermost (<1–2 m) sea surface layer⁹. Furthermore, in the Caribbean part of the western Atlantic, the dominant source of multi-annual upper ocean surface temperature variability is from global atmospheric forcing, with little direct influence (Extended Data Fig. 2) from other ‘natural modes’ of internal variability, such as the Atlantic Meridional Overturning Circulation (AMOC)¹⁷. Thus, temperature changes in the Caribbean OML appear to be mainly driven by external radiative forcing, which makes this an ideal region to monitor global trends in SSTs^{9,17}.

Results

Coralline sclerosponges are an ancient lineage of calcifying sponges¹⁸, typically found in light-limited cryptic marine environments that extend from the relatively uniform temperature regime of the OML to below the thermocline. In this study, specimens of *Ceratoporella nicholsoni*¹⁸ were specifically targeted from within the OML of the eastern Caribbean, along the steeply dipping insular slope, offshore Puerto Rico and the nearby island of St Croix (Extended Data Fig. 3). The ages and growth rates of specimens collected from 2007 to 2017 were determined using sensitive ²³⁰Th/²³⁸U-series analyses¹⁹ back to the 1850s, with several to the beginning of the 1700s (Methods). Ambient seawater temperatures were derived from measurements of Sr/Ca

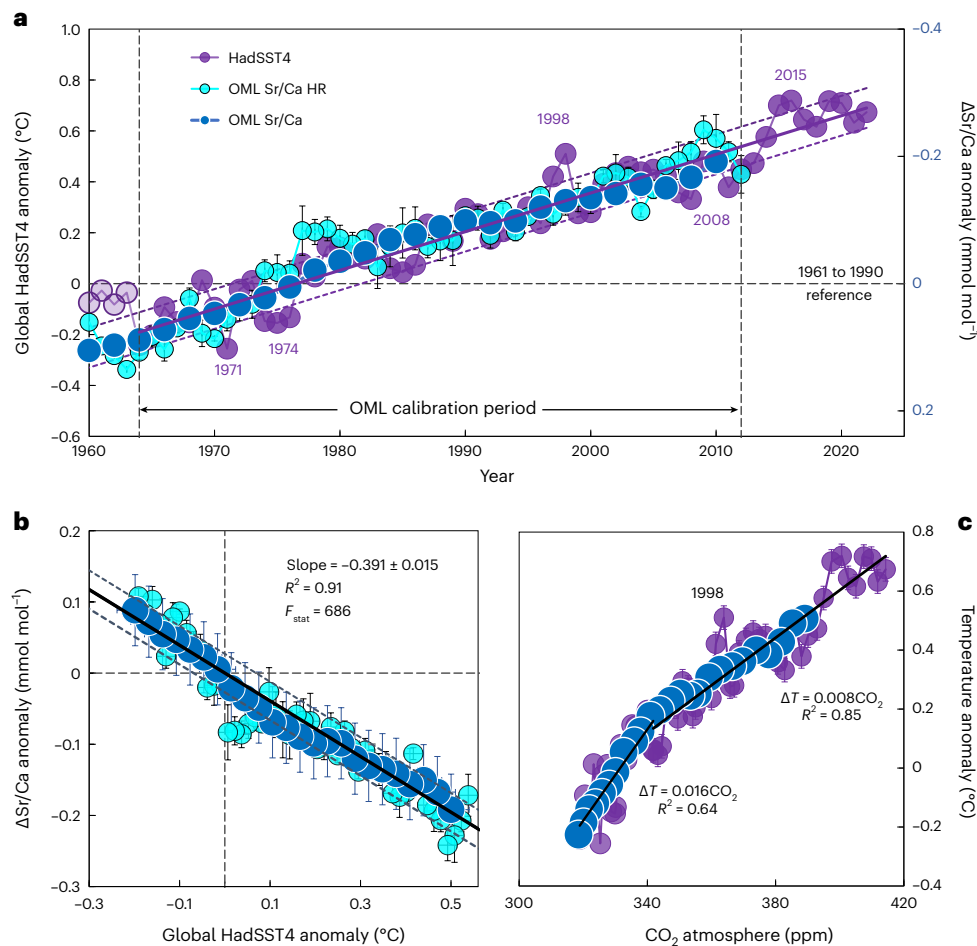


Fig. 3 | Calibration of $\Delta\text{Sr}/\text{Ca}$ against modern SST anomalies. a, Left axis, global mean HadSST4 (ref. 13) anomalies referenced to 1961–1990 with solid line showing linear regression versus time (Extended Data Fig. 4a). Right axis sclerosponge $\Delta\text{Sr}/\text{Ca}$ (mmol mol⁻¹) 2 yr (dark blue) and annually averaged (light blue circles) anomalies from high-resolution (2 month) sampling. **b**, Correlation of $\Delta\text{Sr}/\text{Ca}$ anomalies with linear global HadSST4 array where: $\Delta\text{Sr}/\text{Ca} = -10.391$

(HadSST4) with $R^2 = 0.91$, LINEST $F_{statistic} = 780$ and dashed lines showing 1 s.d. of average residuals (± 0.07 °C). Dotted horizontal and vertical lines are 1961–1990 anomaly means about which the regressions pivot. **c**, Correlations of HadSST4 and OML with atmospheric CO₂ concentrations with the temperature sensitivity to CO₂ halving since 1984. Unless shown, uncertainties for data points are smaller than symbol size (Supplementary Data).

ratios^{20,21} of 0.5 mm (~ 2 yr) continuous increments (Fig. 2a), from the outermost layer down along the growth axis of the progressively older calcium carbonate (aragonite) skeletons (Methods). The absence of seasonal aliasing was confirmed by high-resolution 0.05 mm (~ 2 month) sampling of a specimen between 1960 and 2017, which showed little seasonal variation (Extended Data Fig. 4b) and was therefore averaged to 1 yr resolution.

Over the last ~ 300 yr, all specimens show subparallel arrays of Sr/Ca ratios (Fig. 2a), indicative of the same proportionate response to changes in ambient seawater temperature. However, the offsets between the arrays indicate limited depth-dependent temperature differences, together with some biological induced vital effects. Vital effects are a common feature of biological systems^{21,22} and here the constant offsets were corrected by normalizing the Sr/Ca ratios to the mean of the 1961–1990 reference period for each specimen. The resultant, highly coherent array of stacked 2 yr $\Delta\text{Sr}/\text{Ca}$ anomalies (Fig. 2b) thus indicates a constant sensitivity of the specimens to differential changes in temperature (that is, anomalies).

Calibration of sclerosponge Sr/Ca OML temperatures

To determine the temperature sensitivity of sclerosponge $\Delta\text{Sr}/\text{Ca}$ anomalies, the 2 and 1 yr averaged arrays were compared with global mean SSTs (HadSST4)¹³ from 1964 to 2012 inclusive. Following established

procedures²³, the global average HadSST4 anomalies were detrended using a well-defined ($R^2 = 0.91$) linear relationship, with the residuals being mainly due to periods of high ENSO variability (Extended Data Fig. 4a). The modern (1964–2012) $\Delta\text{Sr}/\text{Ca}$ OML anomalies were then regressed against the linear global HadSST4 (Fig. 3a,b), which assumes that the ~ 50 yr OML $\Delta\text{Sr}/\text{Ca}$ record incorporates a large fraction of the well-defined increase in modern global SSTs. This yields a slope of -0.391 ± 0.015 mmol °C⁻¹, with the calibration period representing nearly one-half of the total amount global warming that has occurred to date.

Although the $\Delta\text{Sr}/\text{Ca}$ anomalies show the expected thermodynamic-based²⁴ negative correlation with global SSTs, the temperature sensitivity is greater than previous studies^{25,26}, including those of scleractinian corals^{20,21}. However, previous attempts to calibrate the temperature sensitivity of Sr/Ca ratios in sclerosponges^{25,26} have been based on either depth-dependent differences in temperature that incorporate vital effects^{25,26} or, alternatively, a lower precision laser-ICP seasonal study²⁷ within the actively calcifying tissue zone. The constant, high sensitivity of $\Delta\text{Sr}/\text{Ca}$ temperature anomalies (± 0.07 °C) in *C. nicholsoni*, found here for many specimens, is attributed to multistage regenerative calcification as seawater is pumped and exchanged within the active (~ 0.5 –1 mm) calcification zone, which extends from the uppermost surface to lower basal zone¹⁸. This also accounts for the absence of a

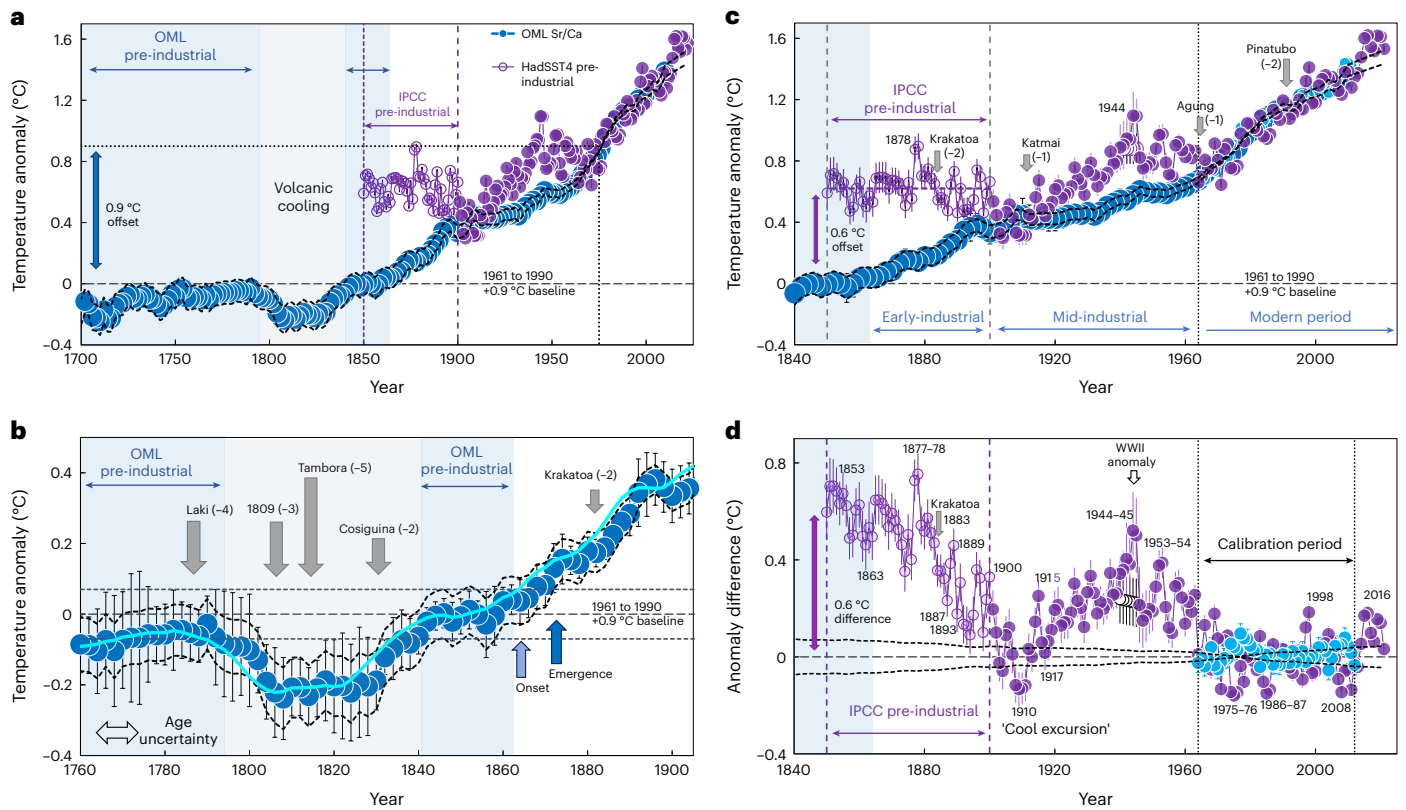


Fig. 4 | OML and HadSST4 global mean anomalies. **a**, Comparison of OML and HadSST4 (ref. 13) records with offsets of 0.9 ± 0.1 °C to account for warming from the pre-industrial period (blue shading from the 1700 to early 1790s and 1840 to early 1860s) to the 1961–1990 anomaly reference mean (vertical dotted line). **b**, Timing of major volcanic eruptions denoted by grey arrows with negative radiative forcing (W m^{-2}) (ref. 16). Onset of industrial warming in mid-1860s

(light blue arrow) followed by emergence in early 1870 (blue arrow). Error bars are 2 s.e.m. (Supplementary Fig. 1) with light blue line showing 5-year moving average. **c**, Comparison of OML and IPCC pre-industrial values with mean offset of ~ 0.6 °C. Horizontal arrows show stages of industrial-era warming. **d**, Difference between sclerosponge OML and HadSST4 anomalies with El Niño years shown in italics. Open symbols show national fleet corrections³⁷.

seasonal signal in either the ~ 2 month sampling (Extended Data Fig. 4b) or the 2 yr stacked arrays (Fig. 2b). This, together with the low sensitivity of Caribbean OML to central Pacific generated ENSO teleconnections^{9,28}, accounts for the limited ENSO variability in the sclerosponge OML record with, for example, the main 1997–98 El Niño being absent.

Calibration of the sclerosponge Sr/Ca palaeothermometer against global temperature changes thus provides strong empirical evidence that the Caribbean OML has warmed proportionately to the average global increase in SST, over the last ~ 50 yr. This finding is supported by modelling^{9,17,29} which shows that, across this broad central western Atlantic region, SSTs have also increased at approximately the same rate as the global average (Extended Data Fig. 2)¹⁷. This can be understood as anthropogenic imposed radiative heating being an essentially passive tracer in the Caribbean OML²⁹, whereas in the northern Atlantic, global warming plays an active role in modifying AMOC¹⁷ and hence heat uptake in that region. Thus, our empirical findings are consistent with the Caribbean being ideally positioned to monitor at-scale global greenhouse warming with minimal superimposed changes from AMOC¹⁷, whilst still registering the broader effects of ENSO teleconnections²⁸. Importantly, modelling¹⁷ also provides a strong physical basis for extending the modern (1964–2012) calibration of the sclerosponge Sr/Ca palaeothermometer back to the eighteenth to nineteenth centuries, when still rudimentary instrumental measurements of SSTs were either absent or, at best, limited in geographic coverage (Extended Data Fig. 1)^{8,9}.

Pre-industrial period and onset of industrial-era warming

The three centuries of OML temperature changes preserved in the skeletons of long-lived Caribbean sclerosponges (Fig. 4) show that the

pre-industrial baseline period is defined by the same essentially constant (< 0.1 °C decade⁻¹) temperatures from 1700 to 1790 and then from 1840 to the early 1860s. The intervening period is marked by prolonged global-scale cooling (Fig. 4a,b), consistent with high concentrations of volcanic-generated sulfate aerosols found in ice cores⁷. This includes major volcanic eruptions (Fig. 4b) in 1783 (Laki), 1809 (unknown), 1815 (Tambora) and 1832 (Cosiguina). The most important is the Tambora eruption in Indonesia during 1815³⁰, the largest explosive event yet recorded in ‘living’ history³¹. This caused ‘The Year without a Summer’ in 1816^{7,30}, with the global-scale cooling (-0.2 ± 0.06 °C) being evident in the Caribbean OML record from 1808 to 1828, with a gradual return to warmer pre-industrial levels during the 1830s (Fig. 4b). The final stage of the pre-industrial period is thus defined by the plateau in temperatures between 1840 and the early 1860s, at marginally warmer (~ 0.1 °C) pre-industrial temperatures compared to the 1700s. The sclerosponge record (Fig. 4b) of these well-known historic events^{7,30,31} thus confirms the veracity of the Caribbean $\Delta\text{Sr/Ca}$ OML thermometer as a recorder of globally forced radiative temperature changes. As expected⁹, temperature changes in the OML are dampened relative to the atmosphere due to the much greater heat capacity of the OML (Fig. 5a).

Relative to this extended and now well-defined pre-industrial baseline, an offset of 0.9 ± 0.1 °C is applied (Fig. 4) to account for the temperature increase from the pre-industrial baseline period (that is, mean temperatures from 1700 to 1790 and from 1840 to 1860) to the 1961–1990 anomaly reference period. On this basis, the onset of industrial-era warming is evident by the mid-1860s. Although earlier than the IPCC estimate¹⁰ (Fig. 4b,c), it is in good agreement with previous palaeoclimate reconstructions^{32,33} that indicate an ‘early’

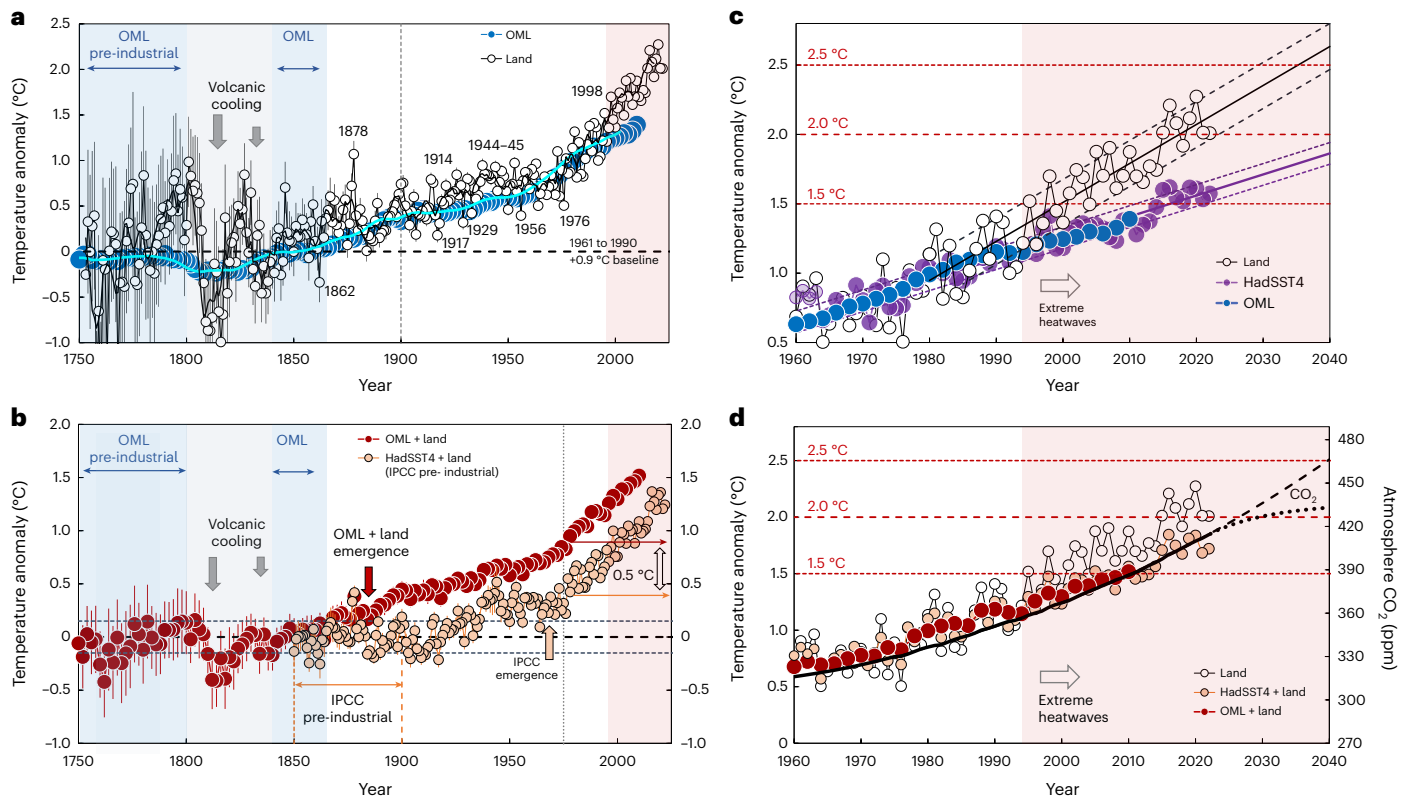


Fig. 5 | OML and GMSTs. Anomalies relative to 1961–1990 baseline with +0.9 °C offset (unless indicated). **a**, OML and Berkeley land¹² temperature anomalies with onset of extreme land-air temperature from about 1990 (pink shading). **b**, GMSTs from blended OML and land¹² anomalies (this study dark red circles) and from blended HadSST4 and land temperatures¹³ (orange circles), the latter relative to IPCC 1850–1900 pre-industrial period, which underestimates global warming by ~0.5 °C. See refs. 11–13 and Supplementary Data for uncertainties.

c, OML and HadSST4 of >1.5 °C and land >2 °C temperature increases by 2020. **d**, GMST records for blended OML + land and blended HadSST4 + land with 1.5 °C passed during 2012–2015. At current rates of emissions 2 °C global warming will be reached by late 2020s. Historic evolution of atmospheric CO₂ (solid line), future increases with present-day rates of emissions (dashed line) and 10% annual reductions from 2025 to halve emissions by early 2030 (dotted line).

mid-nineteenth-century onset of industrial-era warming. This is especially the case if account is taken of the now much improved resolution of our OML record, which clearly distinguishes the initiation of early industrial warming in the mid-1860s from the prolonged recovery that followed the early 1800s global-scale volcanic cooling. Thus, the emergence of OML warming is apparent by the mid-1870s (Fig. 4b), with emergence being defined by the more stringent criteria of warming that first exceeds and remains 2σ above the pre-industrial warming³⁴. This is more than 80 years earlier than instrumental SST records⁸ (Fig. 4c) or shallow-water palaeoclimate coral records in which high natural variability masks the emergence of industrial-era warming until the mid twentieth century^{32,33} (Fig. 5b).

OML temperatures over the industrial era

On the basis of the sclerosponge OML record, industrial-era warming can be categorized into three broad stages (Fig. 4c). The first is the early industrial period from the mid-1860s to early 1900s, when temperatures increased by 0.3 ± 0.1 °C at an average rate of $\sim 0.09 \pm 0.03$ °C decade⁻¹. This was followed by a similar amount of warming (~ 0.3 °C) from the early 1900s to the early 1960s (the mid-industrial period) but at nearly half the average rate (0.04 ± 0.02 °C decade⁻¹). Finally, starting from the mid-1960s (the ‘modern’ period) temperatures increased at a much faster rate of 0.15 ± 0.05 °C decade⁻¹ (Fig. 4c) in response to rapidly increasing atmospheric CO₂. Since the mid-1980s, the temperature sensitivity to increasing CO₂ has halved, from $\sim 0.17 \pm 0.02$ °C per 10 ppm CO₂ during 1964–1984 to the present-day (1985–2020) 0.08 ± 0.02 °C per 10 ppm CO₂ (Figs. 3c and 4c). While the causes of

this decrease in the sensitivity of OML warming to CO₂ require further investigation, we note that it is difficult to reconcile with the cooling effects of industrial aerosols¹⁶ but it does coincide with the global increase in summertime mixed-layer depths³⁵ and hence greater heat capacity of the OML.

In contrast to this coherent pattern of OML warming, ship-based records of SSTs (for example, HadSST4)¹³ show much greater ‘roller-coaster’ like variability, with periods of rapid warming followed by falling temperatures (Fig. 4). Most notable is the period from 1850 to 1880, the first part of the IPCC pre-industrial reference period, that is characterized by unusually warm temperatures, especially during the 1877–78 El Niño³⁶. Then, from around 1880 until the early 1900s, SSTs cooled in a series of steps with only the first being attributable to cooling from the Krakatau eruption in 1883 (Fig. 4c,d). By the early 1900s and especially during the so-called 1908 to 1910 ‘cool excursion’, there is good agreement between the OML and HadSST4 records. Paradoxically, during the IPCC 1850–1900 pre-industrial period¹⁰ (Fig. 4c), temperatures were ~ 0.3 °C anomalously warmer than the beginning of the twentieth-century ‘industrial era’ despite increasing atmospheric CO₂.

While there is good agreement between the OML and HadSST4 records during the early 1900s (Fig. 4), HadSST4 is again warmer during the mid-1920s and especially during the mid-1940s World War II period (Fig. 4c,d). The latter discrepancy is attributed to changes from bucket to engine-room water intake measurements^{8,9}, as well as recently identified biases between different national fleets³⁷. It is uncertain, however, whether these and the much more significant offsets during the IPCC pre-industrial period are due, for example, to an over-representation

of warm El Niño events in the poorly constrained nineteenth-century ICOADS records¹⁵ or to greater natural variability in ENSO before 1960, although our OML record suggests the former.

Discussion

Understanding how greenhouse forced warming has affected land-air temperatures relative to the much larger heat sink of the upper ocean remains a challenge. Here, we assume that, relative to the 1961–1990 reference period, the same fixed offset of 0.9 °C can be applied to land-air as well as the OML anomalies (Figs. 4 and 5), although there are larger uncertainties¹² in land-based records from 1750 to 1860 (Fig. 5a). Despite this limitation, there is nevertheless good agreement between the land-air and OML records, especially during the historically well-documented Tambora eruption when volcanic aerosols induced global cooling. Significantly, from mid-1860 to 1900, both land and OML temperatures increased synchronously by ~0.3 °C. Conversely, over the same IPCC 1850–1900 pre-industrial period, HadSST4 is initially up to 0.6 °C warmer (Fig. 4c) followed by an anomalous cooling trend compared to the well-defined OML and land records of consistent warming from the 1860s. Our findings now resolve the ‘warm-land cool-ocean’ conundrum posed by using the IPCC^{10,16} pre-industrial reference period (Fig. 1b). Hence modern observations should continue to be referenced to the 1961–1990 mean (Fig. 1a) but with an adjustment of +0.9 °C to account for the temperature increase since the onset of industrial-era warming in the mid-1860s to the 1961–1990 mean (Fig. 4a). On this basis, the land and SST records have shown a generally coherent response to ENSO up until the 1990s, characterized by relatively warmer land temperatures during strong El Niño and cooler temperatures during La Niña events (Fig. 5a).

Importantly, however, the long-term similarity in rates of land and upper ocean surface warming starts to breakdown in the late twentieth century, with land-air temperatures now increasing at nearly twice the rate of the surface oceans regardless of the ENSO phase (Fig. 5a,c). Rather than the land-air record being part of an ongoing post-1900s warming trend relative to the IPCC 1850–1900 pre-industrial period, as currently assumed¹⁶ (Fig. 1b), our findings show a distinct divergence from the surface ocean from around 1980–1990 (Fig. 5a,c). This is consistent with the already well-documented amplified warming of the high-latitude Northern Hemisphere land masses and the decline of Arctic permafrost^{38,39}. This change also coincides with the increased frequency of both Southern Hemisphere and Northern Hemisphere heatwaves² and associated extreme events, such as droughts and wildfires⁴⁰. Wildfires and more frequent bushfires are also an additional source of atmospheric CO₂, providing an enhanced feedback mechanism. Although the relative importance of the regional and global processes driving the increased frequency and intensity of land-based heatwaves is still uncertain³⁹, our revised record of industrial-era warming now clearly shows that terrestrial environments have been subject to a much faster rate of warming since the 1990s, compared to those in the more stable OML of the upper surface oceans.

These findings also have important implications for near-term projections of global warming. As already described, relative to the 1961–1990 reference, OML and land temperatures (Fig. 5a) and hence GMSTs (Fig. 5b) increased by $\sim 0.9 \pm 0.1$ °C since the 1700–1860 pre-industrial period. This compares with only ~ 0.4 °C when HadSST4 and land temperatures are estimated relative to the IPCC 1850–1900 pre-industrial period¹⁰, a difference of 0.5 °C (Fig. 5b). The additional 0.5 °C in global warming above IPCC estimates¹ also implies that GMSTs were $\sim 1.7 \pm 0.1$ °C above 1700–1860 pre-industrial levels by 2018–2022, compared to the IPCC estimate¹ of $\sim 1.2 \pm 0.1$ °C (Fig. 5b). Thus, the opportunity to limit global warming to no more than 1.5 °C by emission reductions alone has now passed and at current emission rates, the 2 °C threshold for GMSTs will be reached by the late 2020s (Fig. 5d).

We have shown that the late-twentieth-century land-air temperatures have been increasing at almost twice the rate of the surface oceans

and are now ~ 2 °C above pre-industrial levels. If these current rates of warming continue, mean land temperature will exceed 2.5 °C by about 2035, with GMSTs expected to follow in early 2040 (Fig. 5c,d). Consequently, the overriding aim of the UN Paris agreement to keep the combined land and ocean global surface temperature increase to below 2 °C is now a much greater challenge, emphasizing the even more urgent need to halve emissions by 2030.

Online content

Any methods, additional references, Nature Portfolio reporting summaries, source data, extended data, supplementary information, acknowledgements, peer review information; details of author contributions and competing interests; and statements of data and code availability are available at <https://doi.org/10.1038/s41558-023-01919-7>.

References

1. *IPCC Climate Change 2023: Synthesis Report* (eds Core Writing Team, Lee, H. et al.) (IPCC, 2023).
2. Russo, E. & Domeisen, D. I. Increasing intensity of extreme heatwaves: the crucial role of metrics. *Geophys. Res. Lett.* **50**, e2023GL103540 (2023).
3. Adoption of the Paris Agreement FCCC/CP/2015/L.9/Rev.1 (UNFCCC, 2015); https://unfccc.int/sites/default/english_paris_agreement.pdf
4. Domeisen, D. I. V. et al. Prediction and projection of heatwaves. *Nat. Rev. Earth Environ.* **4**, 36–50 (2023).
5. Hawkins, E. et al. Estimating changes in global temperature since the preindustrial period. *Bull. Am. Meteorol. Soc.* **98**, 1841–1856 (2017).
6. Etheridge, D. et al. Natural and anthropogenic changes in atmospheric CO₂ over the last 1000 years from air in Antarctic ice and firn. *J. Geophys. Res.* **101**, 4115–4128 (1996).
7. Gao, C., Robock, A. & Ammann, C. Volcanic forcing of climate over the past 1500 years: an improved ice core-based index for climate models. *J. Geophys. Res.* **113**, D23111 (2008).
8. Kent, E. C. & Kennedy, J. J. Historical estimates of surface marine temperatures. *Annu. Rev. Mar. Sci.* **13**, 283–311 (2021).
9. Deser, C., Alexander, M. A., Xie, S.-P. & Phillips, A. S. Sea surface temperature variability: patterns and mechanisms. *Annu. Rev. Mar. Sci.* **2**, 115–143 (2010).
10. *IPCC Special Report on Global Warming of 1.5 °C* (eds Masson-Delmotte, V. et al.) (WMO, 2018).
11. Morice, C. P. et al. An updated assessment of near-surface temperature change from 1850: the HadCRUT5 data set. *J. Geophys. Res.* **126**, e2019JD032361 (2021).
12. Rohde, R. A. & Hausfather, Z. The Berkeley Earth Land/Ocean temperature record. *Earth Syst. Sci. Data* **12**, 3469–3479 (2020).
13. Kennedy, J. J., Rayner, N. A., Atkinson, C. P. & Killick, R. E. An ensemble data set of sea surface temperature change from 1850: the Met Office Hadley Centre HadSST. 4.0. 0.0 data set. *J. Geophys. Res.* **124**, 7719–7763 (2019).
14. Huang, B. et al. Extended reconstructed sea surface temperature, version 5 (ERSSTv5): upgrades, validations and intercomparisons. *J. Clim.* **30**, 8179–8205 (2017).
15. Freeman, E. et al. ICOADS Release 3.0: a major update to the historical marine climate record. *Int. J. Climatol.* **37**, 2211–2232 (2017).
16. Gulev, S. K. et al. In *Climate Change 2021: The Physical Science Basis* (eds Masson-Delmotte, V. et al.) Ch. 2 (IPCC, Cambridge Univ. Press, 2021).
17. Caesar, L., Rahmstorf, S., Robinson, A., Feulner, G. & Saba, V. Observed fingerprint of a weakening Atlantic Ocean overturning circulation. *Nature* **556**, 191–196 (2018).
18. Willenz, P. & Willenz, P. Micromorphology and ultrastructure of Caribbean sclerosponges. I. *Ceratoporella nicholsoni* and *Stromatospongia norae* (Ceratoporellidae: Porifera). *Mar. Biol.* **103**, 387–401 (1989).

19. McCulloch, M. T. & Mortimer, G. E. Applications of the ^{238}U – ^{230}Th decay series to dating of fossil and modern corals using MC-ICPMS. *Aust. J. Earth Sci.* **55**, 955–965 (2008).
20. McCulloch, M. T., Gagan, M. K., Mortimer, G. E., Chivas, A. R. & Isdale, P. J. A high-resolution Sr/Ca and $\delta^{18}\text{O}$ coral record from the Great-Barrier-Reef, Australia and the 1982–1983 El-Nino. *Geochim. Cosmochim. Acta* **58**, 2747–2754 (1994).
21. D’Olivo, J. P., Sinclair, D. J., Rankenburg, K. & McCulloch, M. T. A universal multi-trace element calibration for reconstructing sea surface temperatures from long-lived Porites corals: removing ‘vital-effects’. *Geochim. Cosmochim. Acta* **239**, 109–135 (2018).
22. Weiner, S. & Dove, P. M. An overview of biomineralization processes and the problem of the vital effect. *Rev. Mineral. Geochem.* **54**, 1–29 (2003).
23. Hawkins, E. et al. Observed emergence of the climate change signal: from the familiar to the unknown. *Geophys. Res. Lett.* **47**, e2019GL086259 (2020).
24. Gaetani, G. A. & Cohen, A. L. Element partitioning during precipitation of aragonite from seawater: a framework for understanding paleoproxies. *Geochim. Cosmochim. Acta* **70**, 4617–4634 (2006).
25. Haase-Schramm, A. et al. Sr/Ca ratios and oxygen isotopes from sclerosponges: temperature history of the Caribbean mixed layer and thermocline during the Little Ice Age. *Paleoceanography* **18**, 1073 (2003).
26. Waite, A. J., Swart, P. K., Rosenheim, B. E. & Rosenberg, A. D. Improved calibration of the Sr/Ca–temperature relationship in the sclerosponge *Ceratoporella nicholsoni*: re-evaluating Sr/Ca derived records of post-industrial era warming. *Chem. Geol.* **488**, 56–61 (2018).
27. Rosenheim, B. E. et al. High-resolution Sr/Ca records in sclerosponges calibrated to temperature in situ. *Geology* **32**, 145–148 (2004).
28. Cai, W. et al. Pantropical climate interactions. *Science* **363**, eaav4236 (2019).
29. Marshall, J. et al. The ocean’s role in the transient response of climate to abrupt greenhouse gas forcing. *Clim. Dynam.* **44**, 2287–2299 (2015).
30. Brohan, P. et al. Constraining the temperature history of the past millennium using early instrumental observations. *Climate* **8**, 1551–1563 (2012).
31. Newhall, C. G. & Self, S. The Volcanic Explosivity Index (VEI): an estimate of explosive magnitude for historical volcanism. *J. Geophys. Res.* **87**, 1231–1238 (1982).
32. Abram, N. J. et al. Early onset of industrial-era warming across the oceans and continents. *Nature* **536**, 411–418 (2016).
33. Tierney, J. E. et al. Tropical sea surface temperatures for the past four centuries reconstructed from coral archives. *Paleoceanography* **30**, 226–252 (2015).
34. Hawkins, E. & Sutton, R. Time of emergence of climate signals. *Geophys. Res. Lett.* **39**, L01702 (2012).
35. Sallée, J.-B. et al. Summertime increases in upper-ocean stratification and mixed-layer depth. *Nature* **591**, 592–598 (2021).
36. Gergis, J. L. & Fowler, A. M. A history of ENSO events since AD 1525: implications for future climate change. *Clim. Change* **92**, 343–387 (2009).
37. Chan, D. & Huybers, P. Correcting observational biases in sea surface temperature observations removes anomalous warmth during World War II. *J. Clim.* **34**, 4585–4602 (2021).
38. Natali, S. M. et al. Large loss of CO_2 in winter observed across the northern permafrost region. *Nat. Clim. Change* **9**, 852–857 (2019).
39. *IPCC Climate Change 2022: Impacts, Adaptation, and Vulnerability* (eds Pörtner, H.-O. et al.) (IPCC, 2022).
40. Bousfield, C. G., Lindenmayer, D. B. & Edwards, D. P. Substantial and increasing global losses of timber-producing forest due to wildfires. *Nat. Geosci.* **16**, 1145–1150 (2023).
41. Keeling, C. D. et al. *Exchanges of Atmospheric CO_2 and $^{13}\text{CO}_2$ with the Terrestrial Biosphere and Oceans from 1978 to 2000. I. Global Aspects* (Scripps Institution of Oceanography, 2001); <https://escholarship.org/uc/item/09v319r9>

Publisher’s note Springer Nature remains neutral with regard to jurisdictional claims in published maps and institutional affiliations.

Open Access This article is licensed under a Creative Commons Attribution 4.0 International License, which permits use, sharing, adaptation, distribution and reproduction in any medium or format, as long as you give appropriate credit to the original author(s) and the source, provide a link to the Creative Commons license, and indicate if changes were made. The images or other third party material in this article are included in the article’s Creative Commons license, unless indicated otherwise in a credit line to the material. If material is not included in the article’s Creative Commons license and your intended use is not permitted by statutory regulation or exceeds the permitted use, you will need to obtain permission directly from the copyright holder. To view a copy of this license, visit <http://creativecommons.org/licenses/by/4.0/>.

© The Author(s) 2024

Methods

Samples

Living specimens of the Caribbean sclerosponge *C. nicholsoni* were collected using mixed-gas closed-circuit rebreathers by the University of Puerto Rico-Mayagüez, Department of Marine Sciences technical diving team that includes C. Sherman, M. Carlo, H. Ruíz, M. Nemeth, E. Tuohy, I. Bejarano and D. Kesling. Collections were made from 2007 to 2017 and cover a depth range of ~33 to 91 m. Sampling locations (Extended Data Fig. 3 and Supplementary Table 1) for this study include Bajo de Sico (BS33), Mona Channel, Puerto Rico, the southern insular margin of southwest Puerto Rico off La Parguera (LP36, LP47, LP53, LP58) and offshore the northwest coast of the island of St. Croix, US Virgin Islands (DB91). After collection, the specimens were slabbed into ~5–7 mm thick slices, cleaned in deionized water using an ultrasonic probe in preparation for precisely controlled subsampling (milling) and geochemical analyses conducted at the UWA isotope laboratories.

Initially, samples were subject to high-precision U-series dating¹⁹ (see below) to establish accurate chronologies of skeletal growth. For this purpose, U-series dating was undertaken on (50–100 mg) samples extracted from narrow (~1 mm wide) slots milled adjacent to the sampling for Sr/Ca analyses. The ~1 mm slots were cut at ~10 mm intervals along the growth axis of the precleaned sclerosponge slabs with the top (youngest) sample being extracted immediately below the ~1 mm thick tissue zone. Where there is evidence of bio-erosion and hence a possible growth hiatus (for example, BS33) additional samples were taken above and below to determine any temporal discontinuity (Supplementary Fig. 2a).

For Sr/Ca analyses, to minimize temporal smoothing due to sloping growth bands, an ~2 mm thick ledge was milled along the sample growth axis, adjacent to sampling for U-Th dating. Samples for Sr/Ca analysis were then extracted at continuous 0.50 ± 0.005 mm increments resulting in ~10 mg sample aliquots, using a computer-controlled Zenbot mill. For the most recently collected specimen (LP53), additional samples were collected down along the top ~2 cm (1960–2017) at ultra-high-resolution (0.050 ± 0.005 mm) in continuous increments along an adjacent ~2 mm thick ledge, each sample equivalent to ~2 months of average growth and weighing ~0.5 mg. For both 0.5 and 0.05 mm sampling, the aliquots were extracted continuously down along the machined ledge, maintaining precise location of the drill edge relative to the uppermost surface. When necessary, to minimize temporal smoothing, minor adjustments were made to the orientation of the horizontal sampling ledge so that growth bands remained parallel to the mill axis.

Sr/Ca elemental analyses

Sample powders were dissolved in 0.5 N HNO₃ over several hours and then agitated and centrifuged for 1 min at 3,500 r.p.m. to ensure complete dissolution. Aliquots from the dissolved sample were diluted to provide a representative ~2 ml solution at a precisely determined ~10 ppm Ca concentration for analyses of Sr and Ca using an X-series quadrupole ICPMS²¹. To ensure data quality, internal laboratory standards and the international coral standard JCp-1 were also analysed during the same analytical session as the sclerosponge samples. Multiple measurements of the coral standard JCp-1 at the same 10 ppm Ca concentration over an ~4 yr period gave an average relative standard deviation (RSD) of 0.15% (1σ RSD) corresponding to a mean Sr/Ca value of 8.85 ± 0.02 mmol mol⁻¹ ($n = 30$)²¹. Repeat analysis of sclerosponge samples within the same analytical session typically gave an improved reproducibility of ~0.1% (1σ RSD) consistent with the temperature uncertainties shown in Supplementary Fig. 1. Procedural blanks were processed with sample batches to check for procedural contamination and were below detection limits.

Calibration of Sr/Ca temperature anomalies

As described in the text, Sr/Ca anomalies were calculated relative to the 1961–1990 mean. Thus, for each specimen the Δ Sr/Ca ratio anomalies at time increment t is given by:

$$\Delta\text{Sr}/\text{Ca}_{\text{anom}}(t) = \text{Sr}/\text{Ca}(t) - \text{Sr}/\text{Ca}(1961\text{--}1990)$$

where Sr/Ca(t) is the measured ratio (mmol mol⁻¹) and Sr/Ca(1961–1990) is the mean ratio for the common reference period from 1961 to 1990 (inclusive). To facilitate stacking (averaging) of many specimens, the Sr/Ca_{anom} were then rescaled to 2 yr intervals with minimal extrapolation as the 0.5 mm sampling represented ~1.8–2.5 yr intervals, depending on the specimen growth rate. The 2 yr Sr/Ca anomalies (mmol mol⁻¹) were then stacked (that is, averaged) with uncertainties given by $\times 2$ s.e.m. = $2 \text{ s.d.} / \text{Sqrt}(n)$ where n is the number (3–6) of specimens analysed. For the modern calibration period (1964–2012), annual means were also determined from the ultra-high (0.05 mm) ~2 month incremental sampling of LP53 (Extended Data Fig. 4b). Both the stacked 2 and 1 yr anomalies were regressed against the smoothed (linear) HadSST4 global mean SST anomalies (Extended Data Fig. 4a) for the period 1964–2022. This yielded a slope of $-0.391(\pm 0.015 \text{ s.e.m.})$ mmol °C⁻¹, with the calibration incorporating nearly one-half of the total global warming signal. On the basis of this regression, the average standard deviation of the 2 yr means is ± 0.07 °C, consistent with that expected from combined uncertainties in analyses as well as variability between samples.

U-Th dating of sclerosponges

A critical aspect of this study is the requirement for accurate sclerosponge chronologies. For this purpose high-precision ²³⁸U/²³⁰Th series dating¹⁹ was undertaken on (50–100 mg) samples extracted from the narrow (~1 mm wide) slots (see previous). The U-Th sample powders were dissolved and then spiked with a calibrated solution of ^{233,236}U and ²²⁹Th isotopes¹⁹. The spiked solution was then chemically purified using ion-exchange procedures with the separated U and Th fractions analysed using a NEPTUNE MC-ICPMS following procedures similar to those described by ref. 19.

For the high analytical precision required in this study, the ²³⁰Th/²³⁸U measured ratio was corrected for ingrowth of ²³⁰Th between the time of collection and geochemical analyses, a period which ranged from only several months to nearly a decade. Corrections assuming a constant initial [²³⁰Th/²³²Th]_i were then applied to all U-series samples of the same specimen, with further adjustments to optimize the regression of age (x) versus distance from the outer growth surface. Thus, for each specimen, the age–distance relationship was given by:

$$y = C_0 + C_1x + C_2x^2$$

Here, the outermost surface ($x = 0$) C_0 is defined by the collection age (Supplementary Table 2). Correction for initial ²³⁰Th is the major uncertainty (± 2 yr) in determining the time of calcification and hence growth rate of the skeletal segments, compared to the theoretical precision of <1 yr without corrections for initial ²³⁰Th. The initial [²³⁰Th/²³²Th]_i activity ratios ranged from 1.45 to 2.74, with the largest offset ($\sim 70 \pm 2$ yr) required for the deepest (91 m) sample (DB91), consistent with the commonly observed trend of increased dissolved/particulate ²³⁰Th with increasing depth and hence greater [²³⁰Th/²³²Th]_i. For the larger (>10 cm diameter) older specimens, a simple linear relationship ($y = C_0 + C_1x$) was generally found to provide the best fit with minimal degrees of freedom. For other specimens, a polynomial fit ($C_2 \neq 0$) was required to account for the ontogenetic effect of initially lower extension rate in the early growth phase (Supplementary Table 2). The best fit age–distance isochrons are shown in Supplementary Fig. 2 for each specimen together with an insert showing differences of the individual U-series ages from the isochron. We note that the almost constant growth rate of sclerosponges analysed in this study is in marked contrast with other commonly used climate proxies, such as shallow-water scleractinian corals where there can be a strong but generally variable dependence of growth rate on temperature²¹.

Data availability

Complete datasets are given in the Supplementary Data and also lodged with the NOAA National Centers for Environmental Information

<https://www.ncei.noaa.gov/access/paleo-search/?dataTypeId=4> and Figshare <https://doi.org/10.6084/m9.figshare.22954151>.

Acknowledgements

This work was supported by the awards of an ARC Laureate Fellowship (LF120100049) to M.M. and an ARC Future Fellowship (FT160100259) to J.T. and the ARC Coral Reef Studies Centre of Excellence (CE140100020). Collection of sclerosponges was supported by NOAA-NCCOS grants, NA06NOS4780190, NA09NOS4260243, NA10NOS4260223 and NA11NOS4260184 to the UPRM Caribbean Coral Reef Institute and NSF Award 0738825 to A.W. We thank J. P. D'Olivo, A. Kuret, K. Rankenburg and A.-M. Nisumaa-Comeau for providing technical support at the UWA geochemical laboratories. We greatly appreciated the helpful and encouraging comments provided by colleagues.

Author contributions

M.M. and A.W. designed the project. M.M. wrote the initial draft manuscript. C.S. and the UPRM rebreather dive team collected the samples. M.M. and A.W. undertook initial sample preparation. J.T. oversaw Sr/Ca sample preparation and clean-room chemical

extractions. All authors contributed to manuscript writing and revisions.

Competing interests

The authors declare no competing interests.

Additional information

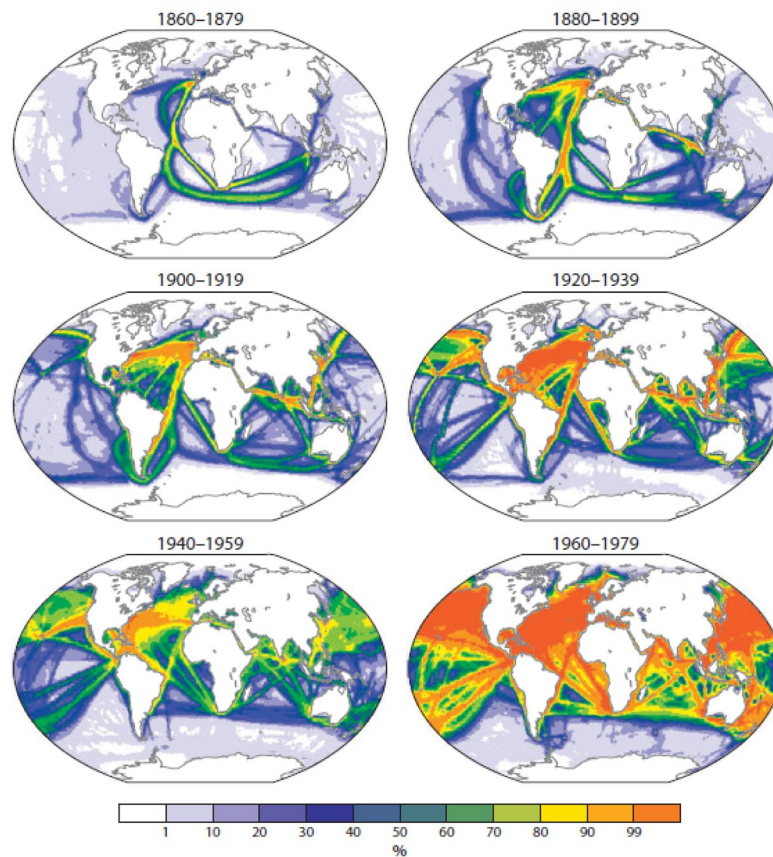
Extended data is available for this paper at <https://doi.org/10.1038/s41558-023-01919-7>.

Supplementary information The online version contains supplementary material available at <https://doi.org/10.1038/s41558-023-01919-7>.

Correspondence and requests for materials should be addressed to Malcolm T. McCulloch.

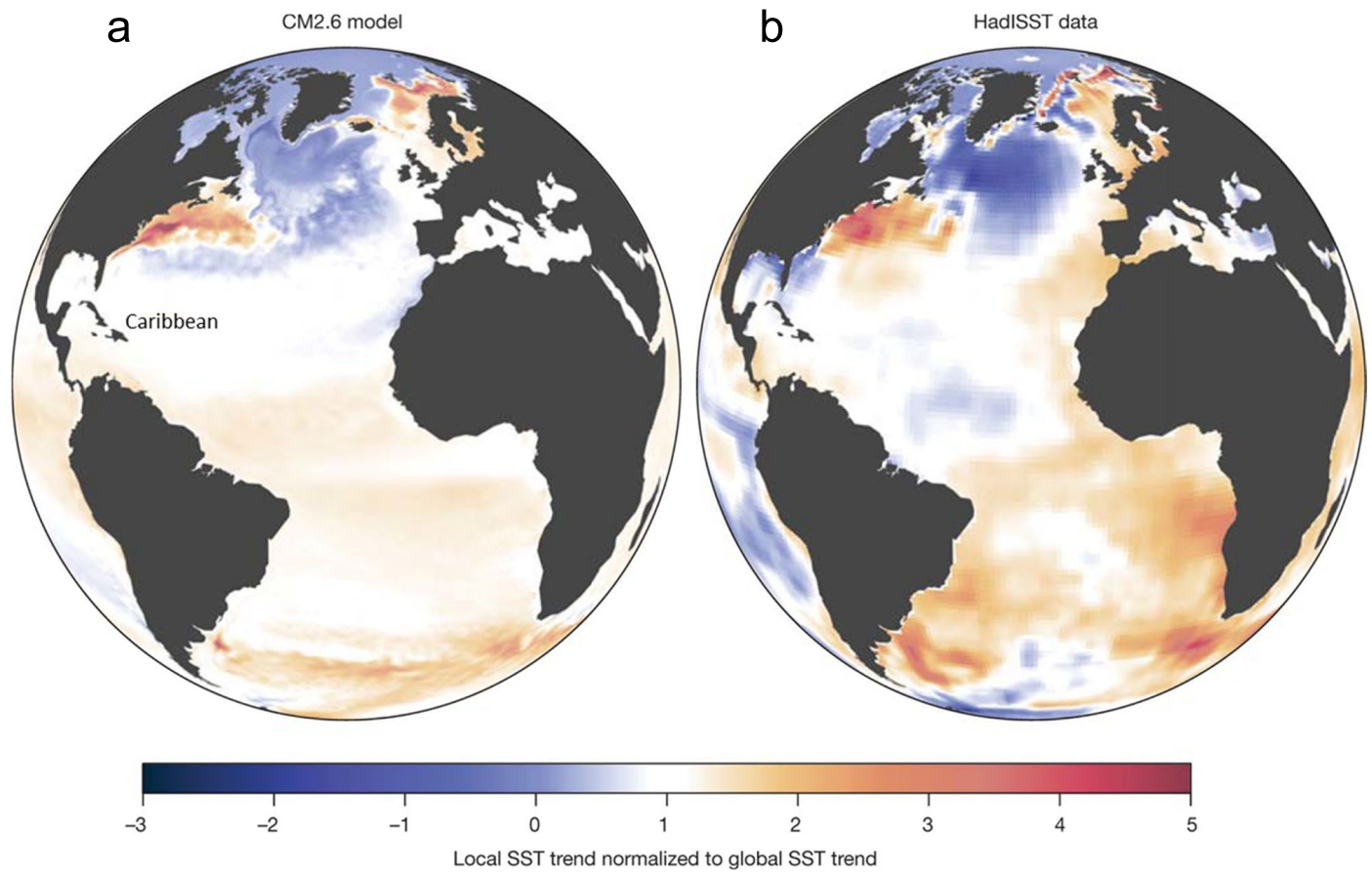
Peer review information *Nature Climate Change* thanks the anonymous reviewers for their contribution to the peer review of this work.

Reprints and permissions information is available at www.nature.com/reprints.



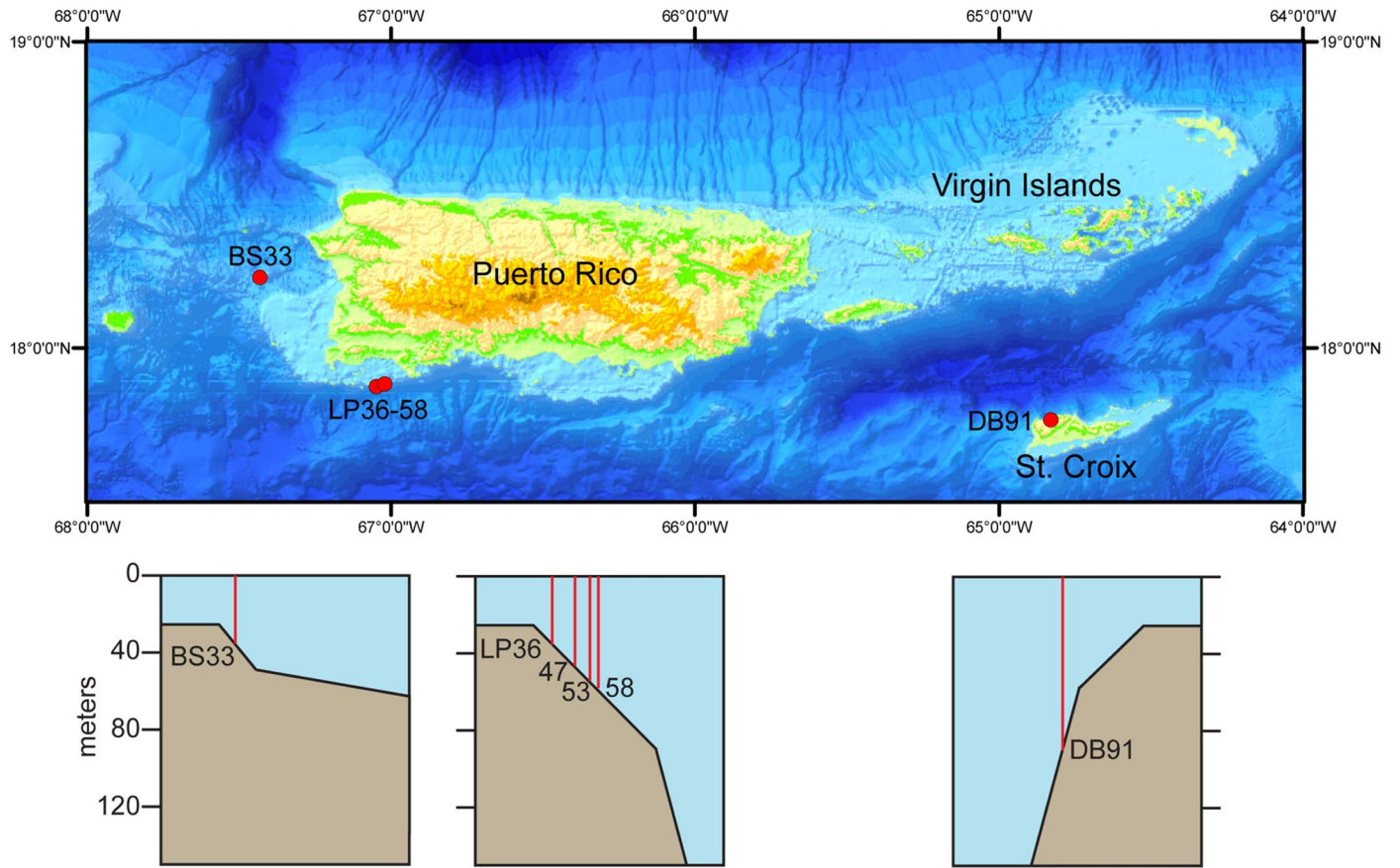
Extended Data Fig. 1 | From Deser et al., 2010⁸ (Fig. 3) showing the distribution of sea surface temperature observations since 1860. Data from the International Comprehensive Ocean Atmosphere Data Set¹⁵ for each 20-year period since 1860. Colour shading indicates the percentage of months with at

least one measurement in a 2° latitude by 2° longitude grid box. Note very sparse observations of especially the critical ENSO regions in the central Pacific Ocean from 1860–1899 with still few observations for the Southern Oceans up to 1980. Figure adapted with permission from ref. 9, Annual Reviews.



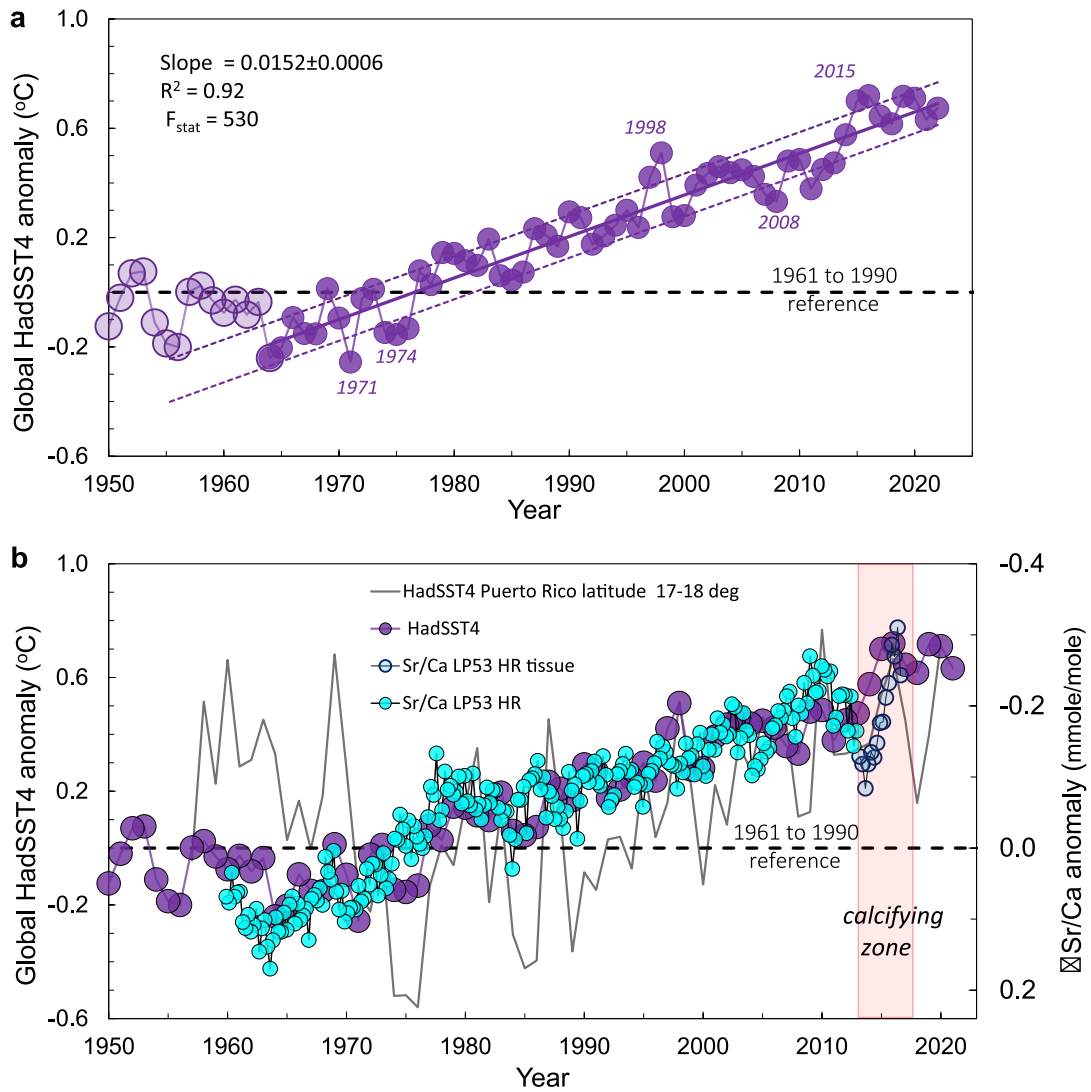
Extended Data Fig. 2 | From Caesar et al.¹⁶. (Fig. 2) showing that the Caribbean SSTs closely following the global mean normalized trend. Data are normalized with the respective global mean SST trends, using the November–May season.

a, Linear SST trends during a CO₂-doubling experiment using the GFDL CM2.6 climate model. b, trends based 1870–2016 (HadISST data). Figure adapted with permission from ref. 17, Springer Nature Limited.



Extended Data Fig. 3 | Map data showing locations and relative sample depths of sclerosponge samples. General locations and water depth profiles from Bajo de Sico (BS), La Parguera (LP) site south-western Puerto Rico and

from Davis Bay (DB) from the island of St. Croix. Map data from the GEBCO Compilation Group (2023) GEBCO 2023 Grid (doi:10.5285/f98b053b-0cbc-6c23-e053-6c86abc0af7b).



Extended Data Fig. 4 | Linear regression of modern global HadSST4 versus time and against OML and atmospheric CO₂. a, Linear (Linest) regression of global HadSST4 versus time from 1964 to 2022 (inclusive) against which the Δ Sr/Ca(t) anomalies are calibrated (see Fig. 3 text). Dashed line show 1SDs of average residuals (± 0.07 °C) from linear regression. b, Comparison of global

average HadSST4 with sclerosponge Δ Sr/Ca(t) ratios for 2-month high-resolution sampling of LP53 showing only limited evidence for seasonality. Active calcification zone is shaded. Grey line shows local gridded SST's offshore La Parguera latitude 17°-18°, longitude 66°-67°.